CHEMISTRY OF MATERIALS

Article

pubs.acs.org/cm

Synthesis of a New Copper-Azobenzene Dicarboxylate Framework in the Form of Hierarchical Bulk Solids and Thin Films without and with Patterning

Jin-Liang Zhuang,[†] Katharina Lommel,[†] Doris Ceglarek,[†] Iryna Andrusenko,[‡] Ute Kolb,[‡] Sandra Maracke,[§] Uta Sazama,[§] Michael Fröba,[§] and Andreas Terfort*,[†]

[†]Institute for Inorganic and Analytical Chemistry, University of Frankfurt, Max-von-Laue-Str. 7, 60438 Frankfurt, Germany

[‡]Institute of Physical Chemistry, Johannes Gutenberg University Mainz, Jakob-Welderweg 11, 55128 Mainz, Germany

[§]Institute of Inorganic and Applied Chemistry, University of Hamburg, Martin-Luther-King-Platz 6, 20146 Hamburg, Germany

Supporting Information

ABSTRACT: Reaction of copper(II) acetate with azobenzene-4,4′-dicarboxylic acid results in the formation of a metal−organic framework with the unexpected stoichiometry of Cu(II):ligand of 2:1. The bulk synthesis results in microspheres assembled from either nanobricks or nanoflakes, depending on the ratio of the reactants in solution. While the former behaves like a bulk solid with clear reflections in the X-ray and electron diffraction experiments, the latter obviously is dominated by surface effects, with a significant fraction of slightly expanded elemental cells and a significantly increased outer surface area. The material could also be deposited on a variety of surfaces using a stepwise layer-by-layer growth, permitting the observation of the changes in composition at each of the deposition steps. The orientation of the crystallites could be influenced by the choice of surface functionalities and their order. When the surfaces became chemically patterned, in this case by microcontact printing (μCP), the deposits could be localized, with the nucleation/growth rate being the determining factor for the preferred growth sites.

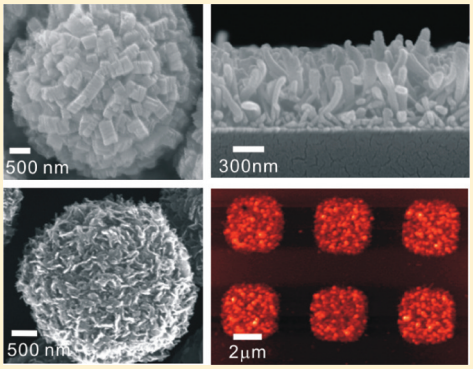

KEYWORDS: *metal−organic frameworks, layer-by-layer, self-assembly, surface patterning*

INTRODUCTION

Metal−organic frameworks (MOFs) are a fascinating class of porous organic−inorganic hybrid materials which already demonstrated potentials for gas storage/separation,[1] heterogeneous catalysis,[2] molecular recognition,[3] and sensing.[4] Since the concept of secondary building units (SBUs) has been introduced for MOF syntheses, various functional properties of MOF materials have been designed and synthesized.[5−7] Typical MOF syntheses involve solvothermal synthesis or slow interdiffusion of the separate solution of the respective building-blocks.[8−11] Recently, nanoscale MOFs have attracted great attention because of promising biomedical applications, such as nitric oxide (NO) storage, drug delivery, biosensing, and bioimaging.[12] To obtain control of the size and morphology of the MOF crystals, other strategies, such as microwave heating,[13,14] ultrasonic synthesis,[15,16] microemulsions,[17,18] as well as solvent-triggered precipitation,[19,20] have been developed. Nanoscale MOFs with various morphologies (e.g., nanospheres,[19,21−23] nanocubes,[24] nanorods,[17] and nanowheels[25]) have been synthesized.[19,26] Lin and co-workers developed a microemulsion technique to prepare nanosized Gd-MOF and Mn-MOF crystals.[17,27] Mirkin et al. and Wang et al. established a solvent-triggered precipitation method to synthesize infinite polymer particles (ICPs).[19,21] Kitagawa and co-workers reported a coordination modulation method using capping reagents to control the crystal growth of nanosized porous coordination polymers (PCPs).[24]

For the application as sensors, smart membranes, catalytic coatings, and many other nanotechnological devices, the deposition of MOFs in form of thin films is essential.[28−33] To grow such MOF films, a number of interesting methods have been employed, including the direct growth/deposition from solvothermal mother solutions,[34,35] the secondary growth on seeding layers,[31,36] the colloidal dip-coating deposition,[37,38] the stepwise layer-by-layer growth,[39−42] the electrochemical deposition,[43] the gel-layer deposition,[44] the combined Langmuir−Blodgett and layer-by-layer method,[45−47] and the spin-coating deposition from a precursor solution.[20,48] For many of these methods, the use of self-assembled monolayers (SAMs) turned out to be a powerful tool to control the lateral structure as well as the crystallographic orientation of the films. In particular, the stepwise layer-by-layer growth method

Received: July 22, 2011
Revised: November 3, 2011
Published: November 7, 2011

established by Wöll and co-workers permits the growth of smooth and homogeneous MOF thin films.[42] A series of well-known MOFs have been grown as thin films on SAM-functionalized surfaces, such as HKUST-1,[42] MOF-508,[39] $M(L)(P)_{0.5}$ (M = Cu, Zn; L = bdc, F_4bdc, ndc; P = dabco, bipy; bdc = 1,4-benzenedicarboxylate, F_4bdc = tetrafluorobenzenedicarboxylate, ndc =1,4-naphthalenedicarboxylate, dabco = 1,4-diazabicyclo[2.2.2]octane, bipy =4,4′-bipyridine).[41] In principle, this method can be extended to grow thin films of any new MOF.

In this paper, we report the preparation of a hitherto unreported MOF, assembled from the Cu-carboxylate dimer SBU and 4,4′-azobenzene dicarboxylate (called Cu-ADA in the following), the morphology of which can be controlled by the exact preparation conditions. In addition, the layer-by-layer method was used to grow this new MOF onto SAM-functionalized surfaces, even in a patterned way.

EXPERIMENTAL SECTION

Synthesis of 4,4′-Azobenzenedicarboxylic Acid (H_2ADA) and Its Salt (ADA^{2-}). H_2ADA (Figure 1) was synthesized according to a previous report.[49] Briefly, the procedure is the following: To a solution of *p*-nitrobenzoic acid (7.0 g, 42 mmol) and NaOH (12.0 g, 0.33 mol) in water (100 mL) a solution of glucose (60 g, 0.33 mol) in water (100 mL) was slowly added at 343 K. After addition, a stream of air was passed through the mixture overnight. The resulting precipitate was filtered, washed with cold water, and dissolved in hot water. The solution was acidified with acetic acid and filtered. The crude product was dried in an oven and purified by dissolution in 150 mL of 1.0 M ammonium hydroxide, filtration, and acidification with acetic acid. The resulting precipitate was collected and dried in an oven. ^{1}H NMR (DMSO-d_6, 300 MHz): 8.19 (d, 4H), 8.04 (d, 4H), 13.31 (br, H).

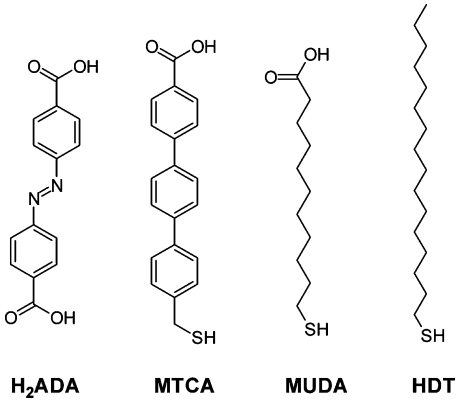

Figure 1. Molecules used in this study.

Because of the very low solubility of H_2ADA in ethanol, we chose an aqueous solution of ADA^{2-} salt as ligand source for the deposition on surfaces. For this, the precipitate that formed after the passage of air was filtered and washed with cold water. Instead of the acidification with acetic acid, the precipitate was recrystallized from hot water. Finally, the precipitate was filtered and washed with cold water, and dried in an oven.

Synthesis of Cu-ADA Hierarchical Crystals. Nanobrick hierarchical MOFs: In an open glass vial, a mixture of a $Cu_2(OAc)_4{\cdot}2H_2O$ solution (5.0 mg in 3 mL of ethanol) and a H_2ADA solution (6.7 mg in 3 mL of dimethylformamide (DMF)) was heated in an oven to 363 K until the ethanol was completely evaporated. The flask was then sealed and kept at the same temperature for another 3 days. After decantation of most of the orange solution, the precipitate was collected by centrifugation followed by three wash steps with ethanol. Finally the sample was dried at 80 °C overnight. Yield: 5 mg. Found: C, 39.51; H, 2.57; N, 6.54%.

Nanoflake hierarchical MOFs: A solution of $Cu_2(OAc)_4{\cdot}2H_2O$ (5.0 mg in 3 mL of ethanol) mixed with H_2ADA (3.4 mg in 3 mL of DMF), the mixture was sealed in a glass vial and left in 363 K oven for 3 days. After most of the dark brown solution was decanted, the precipitate was isolated by centrifugation and washed three times with ethanol. Finally the sample was dried at 80 °C overnight. Yield: 3.1 mg. Found: C, 38.91; H, 2.55; N, 6.35%.

Protein Adsorption onto Cu-ADA MOF. The protocol for protein immobilization on Cu-ADA MOF followed the one in a previous report.[50] A small amount of the respective, dry Cu-ADA powder was dispersed in a PBS-buffer solution (pH 7.4) of 1 mg/mL labeled bovine serum albumin (BSA Alexa Fluor 488 conjugate, Invitrogen, A13100) at 25 °C for two hours. Then the Cu-ADA powder was collected by centrifugation and washed with PBS buffer solution two times. A drop of the remaining slurry was dried on a microscope slide and used for further characterization.

SAM-Functionalized Substrates. The Au substrates were manufactured by electron-beam evaporation of 5 nm of Cr and 40 nm of Au onto four inch Si wafers with (100) orientation. When these films could not be used immediately, they were cleaned by immersion into a 10 mM 1-hexadecanethiol (HDT, Aldrich) solution in ethanol for 2 h followed by a 2 min treatment in H_2 plasma.[51] The clean gold substrates were immersed in either a 1 mM 11-mercaptoundecanoic acid (MUDA, Aldrich) or a saturated 4′-(mercaptomethyl)-terphenyl-4-carboxylic acid (MTCA, synthesized according to ref 52) solution in ethanol for 24 h. The gold substrates with patterned SAMs were fabricated by microcontact printing (μCP) using PDMS stamps either inked with HDT or MUDA (both as 5 mM solutions in ethanol). All substrates were washed with ethanol before the step-by-step growth.

Step-Wise Layer-by-Layer Growth of Cu-ADA Film on Surfaces. The functionalized substrates (or clean bare Au substrate) were alternatingly immersed in a copper acetate solution in ethanol (2 mM) for 20 min and in the ADA^{2-} aqueous solution (0.05 mM) at room temperature for 40 min. Between each step, the substrates were rinsed with ethanol and dried with N_2.

Characterization. SEM images were recorded using a JEOL JSM 7001F scanning electron microscope. Transmission electron microscopy (TEM) and automated diffraction tomography (ADT)[57−59] measurements were carried out with a FEI TECNAI F30 S-TWIN transmission electron microscope working at 300 kV. Scanning transmission electron microscope (STEM) images were taken with a FISCHIONE high angular annular dark field (HAADF) detector and nanoelectron diffraction (NED) patterns were collected with a 1k × 1k slow-scan CCD camera. The use of a 10 μm condenser aperture (C2) enabled a semiparallel illumination of the sample with a 50 nm beam at 0.2 mrad convergence angle. Combined with a high spot size this set up allowed mild illumination conditions reducing the electron dose down to less than 15 $e^-/(Å^2\ s)$. Powder X-ray diffraction (XRD) patterns were collected between 2θ = 2° and 80°, on a STOE θ–θ diffractometer using Cu Kα1 (1.5418 Å) radiation and a linear position-sensitive detector. The XRD measurements were performed in θ/θ mode, with a step width of 0.02°, and a scan rate of 5 s/step for powder samples and 100 s/step for thin film samples. Energy dispersive X-ray (EDX) spectra were recorded on Pentafet link 6446 (Oxford). Atomic Force Microscopy (AFM) measurements were performed on a NanoScope Dimension 3100 atomic force microscope in tapping mode. Thermogravimetric analysis (TGA) was performed on a NETZSCH STA 449F3 under argon atmosphere with a heating rate of 5 K/min. Nitrogen low pressure physisorption isotherms were measured at 77 K using a Quantachrome Autosorb1C apparatus. Ellipsometric measurement was carried out on a SE400 (Sentech Instrument GmbH). FT-IR spectra were recorded with a NICOLET 6700 Fourier Transform Infrared Reflection–Absorption Spectrometer. For bulk substances a diamond ATR cell was used, for thin films on reflective substrates (gold) a modified smart SAGA unit providing an incidence angle of 80° was utilized. SAMs of perdeuterated hexadecanethiol ($C_{16}D_{33}SH$) on gold were used as background samples for thin film FT-IR measurement. Laser scanning

dx.doi.org/10.1021/cm2021092 | Chem. Mater. 2011, 23, 5366–5374

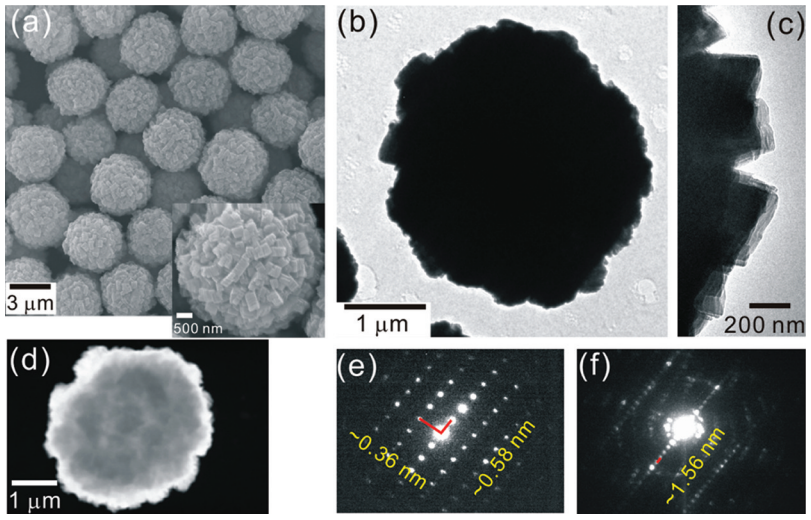

Figure 2. Characterization of nanobrick Cu-ADA spheres. (a) The SEM image demonstrates the hierarchical order of the microspheres, the inset shows a higher magnification. (b, d) TEM and STEM images of single particles. (c) High magnification TEM image of the edge of a microsphere. (e, f) NED patterns of different zones taken from an edge of the nanobricks with some characteristic *d*-distances.

confocal microscopy (LSCM) was carried out on a Zeiss LSM 510 META microscope.

RESULTS AND DISCUSSION

Only a few papers report the successful incorporation of 4,4′-azobenzenedicarboxylic acid (H_2ADA) as a linker in MOFs.[53−56] In our experiments, we also found that under the current conditions we were not able to obtain our compound in the form of single crystals. When using a molar ratio Cu^{2+}/H_2ADA of 1:1, we obtained microspheres with a diameter of 3−4 μm as shown in the scanning electron microscopy (SEM) images (Figure 2a). On closer inspection, these microspheres reveal to be assemblies of nanobricks of about 100−500 nm. To learn more about the structure, we performed transmission electron microscopy (TEM), where the nanobricks became visible at the boundary of the microspheres (Figure 2b). A TEM image with higher magnification (Figure 2c) revealed a layered structure within the nanobricks which appear to be crystalline (Figures 2e,f). Although the SEM and TEM images give an idea about the morphology of the nanobrick microspheres, it was not clear whether the nanobricks only grow on the surface of microspheres or the whole microsphere is assembled by the nanobricks. The gray oversaturated area with many cracks in the scanning transmission electron microscopy (STEM) image (Figure 2d) makes the second assumption more likely.

In contrast to the amorphous microspherical ICPs reported in the literature,[19,21,23] powder XRD (Supporting Information, Figure S1) indicates that the nanobrick microspheres are crystalline. Pronounced diffraction peaks were found at 2θ = 5.66°, 11.36°, 14.29°, 15.52°, and 17.06°, corresponding to lattice plane spacing (*d*-spacing) of 1.56, 0.79, 0.63, 0.57, and 0.52 nm, with the peaks at 11.36° and 17.06° presumably being the second and third order signals of the peak at 5.66°. The *d*-spacing of 1.56 nm correlates well with the length of *trans*-azobenzenedicarboxylic acid. In addition, nanoelectron diffraction (NED) patterns of different zone axes were collected from a thin region on the edge of a single nanobrick from the high magnification TEM image. The regular arrays of sharp spots in the NED patterns confirm the single-crystal nature of the layers building the nanobricks and also render *d*-values of 1.56 nm, 0.58 nm (both similar to the values obtained by PXRD), and additionally 0.36 nm. Since the nanoblock crystals were extremely sensitive to the electron beam, three-dimensional electron diffraction data were collected by automated diffraction tomography (ADT),[57−59] performed with a beam size of 70 nm and under cryo-conditions and low dose illumination. Although the samples were milled, no isolated single crystal could be found, making the ADT acquisition extremely complicated. In addition the collected data sets were weak and partially distorted, presumably because of slight bending of the crystals. Nevertheless, some three-dimensional reciprocal space information (see Supporting Information, Figure S2) could be reconstructed from platelets protruding out from microsphere aggregates, leading to a monoclinic primitive cell with the following parameters: a = 0.366 nm, b = 1.560 nm, c = 0.637 nm, and β = 101.5°. Since no extinctions were observed, the space group of the system is either *P2*, *Pm*, or *P2/m*. Note that the volume of this cell is about the size of a single ADA molecule, limiting the range of possible structural configurations. The accurate structure determination still is a goal of future work.

To learn about the other constituents of the lattice, elemental analysis of the microspheres was performed. The result (C: 39.51%; H: 2.57%; N: 6.54%) suggests that the only organic component is the ADA ligand, since the carbon/nitrogen weight ratio of 6.04 corresponds very well with the one in this ligand (6.01). Assuming that the oxidation state of the copper ion has not changed during the reaction, a composition of $C_{14}Cu_{1.86}H_{10.84}N_2O_{6.28}$ (normalized to 1 ADA formula unit) can be calculated. This formula corresponds very well with the residue found after the heating to 850 K in the DTA-TG experiments, where 34.9% of weight was found, with 34.7% being expected. This residue consisted exclusively of CuO, as confirmed by PXRD. The ratio of Cu(II) to ADA of almost two in the MOF was completely unexpected and hints on a much more complicated structure than anticipated. The excess of hydrogen and oxygen in the formula thus cannot simply be explained by the presence of water, but also involves hydroxide groups attached to the Cu^{2+} ions to warrant charge neutrality.

The molecular formula suggested that starting with a molar ratio of Cu^{2+}/H_2ADA of 2:1 might result in larger, maybe even

dx.doi.org/10.1021/cm2021092 | *Chem. Mater.* 2011, 23, 5366−5374

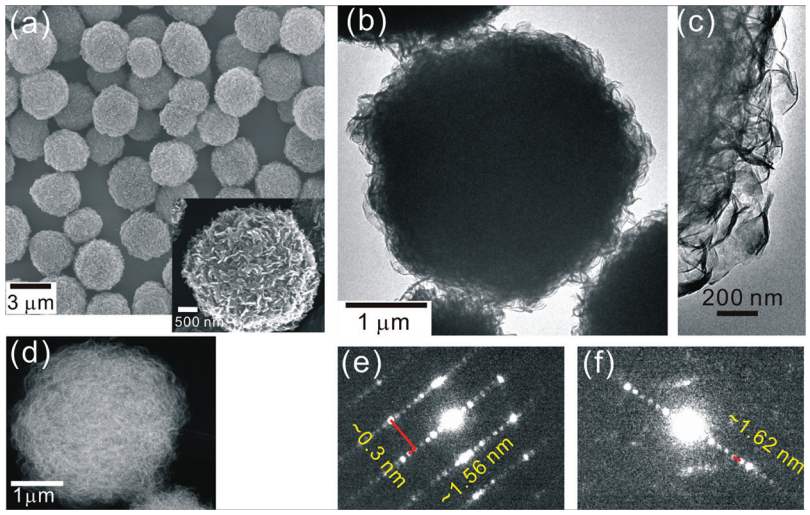

Figure 3. Characterization of the nanoflake hierarchical Cu-ADA MOF. (a) The SEM image again shows the prevalence of two dimensions, that is, the diameter of the microspheres and the thickness of the flakes, the inset shows the structure at higher magnification. (b, d) TEM and STEM images of the microsphere. (c) High magnification TEM image on the edge of the microsphere. (e, f) NED patterns of different zones with some characteristic *d*-distances: (e) from nanoplatelet phase; (f) from the second most abundant phase (nanoflake).

single crystals. Surprisingly, using this ratio did not only result again in the formation of microspheres, but these now consisted of a hierarchical assembly of nanoflakes instead of nanobricks. As shown in Figure 3, the diameter of the nanoflake assemblies is about 2−4 μm, so almost unchanged compared to the previous case, but with a somewhat broader distribution. The thickness of each nanoflake is less than 10 nm as estimated from the high magnification TEM image in Figure 3c. Again, the TEM image could not provide information about the inner structure of the nanoflake Cu-ADA particles since the electrons could not penetrate through the particle, so STEM was used as a first tool to access cross-sectional information. The hairy appearance of the microsphere image (Figure 3d) suggests that the whole microsphere is assembled from the nanoflakes again in a hierarchical manner. The crystallinity of the nanoflakes has been confirmed by PXRD (Supporting Information, Figure S1) and the observation of NED patterns. Note that a closer inspection of the main peak in the PXRD pattern of nanoflake microsphere (see inset in Supporting Information, Figure S1) shows that the main peak (2θ = 5.37°) is not at 2θ = 5.66° anymore, as it was with the nanobricks, but that the latter peak still remains as a shoulder of the former. It can be expected that the larger spacing corresponds to structures at or near the surface of the nanoflakes, where the lattices might be expanded, for example, by hydration or relaxation. The corresponding *d*-values of 1.62 and 1.56 nm, respectively, were also found in the NED patterns, although the blurriness of the white spots is a result of the nanoscopic dimensions of the flakes making an exact determination of the *d*-spacings harder. This problem is worsened by the volatility of the pattern, which disappears within a second, showing that these nanoflake microspheres are again extremely sensitive to the electron beam.

Elemental analysis of the nanoflake microsphere was almost the same as for the nanobrick MOF (C: 38.91%; H: 2.55%; N: 6.35%). The somewhat lowered content of C, H, and N hinted on an empirical formula of $C_{14}Cu_{1.93}H_{10.92}N_2O_{6.39}$ (again normalized to one ADA formula unit), which is again very consistent with the amount of CuO expected after the DTA-TG experiments (expected: 35.5% by weight, found: 35.5%). The increased Cu content of the nanoflakes presumably results from the increase in the Cu^{2+} concentration in the preparation and is accompanied by an increase in the O and H content of the material to compensate for the extra charges.

To explore the inner morphology of the two different kinds of microspheres further, we used the fact that proteins adhere to many inorganic surfaces. Thus, we exposed the two kinds of microspheres to bovine serum albumine (BSA) labeled with a fluorescent dye (AlexaFluor 488). Laser scanning confocal microscopy (LSCM) images in the Supporting Information, Figure S7 show that the protein entered the structure of the nanobrick microspheres and became deposited even within the spheres around the nanobricks. The "cavities" became filled up by the labeled protein, as becomes visible by the fine green dots in the image (a). In contrast to this, the nanoflake structure shows only a ring if a focal plane within the microspheres is chosen. This implies that the inner part of the nanoflake microspheres is not accessible for the protein molecules and they rather become deposited at the outer structure exposed by the thin flakes.

Many MOFs possess large inner surfaces because of their framework structure. Since during the synthesis typically the pores of the frameworks are filled with solvent molecules, these have to be removed before the inner surface can be determined. For this, the MOFs are typically heated in vacuum. The above-mentioned DTA-TG measurements showed that the samples were stable up to 550 K before decomposition occurred (Supporting Information, Figure S5). Thus, the samples were heated in high vacuum to 403 K, 423 K, and 523 K, before the resulting surface areas were determined from the N_2 isothermal sorption at 77 K using the Brunauer−Emmett−Teller (BET) formula (Supporting Information, Figure S6). Independently from the activation temperature, the surface area of the nanobrick microspheres amounted to about 27 $m^2\ g^{-1}$ and the one of the nanoflake spheres to about 132 $m^2\ g^{-1}$, with the latter value becoming diminished to about 107 $m^2\ g^{-1}$ after heating to 523 K. These values strongly hint on adsorption only at the outsides of the nanocrystals, with the nanoflakes providing more surfaces because of their larger surface-to-volume ratio.

dx.doi.org/10.1021/cm2021092 | *Chem. Mater.* 2011, 23, 5366−5374

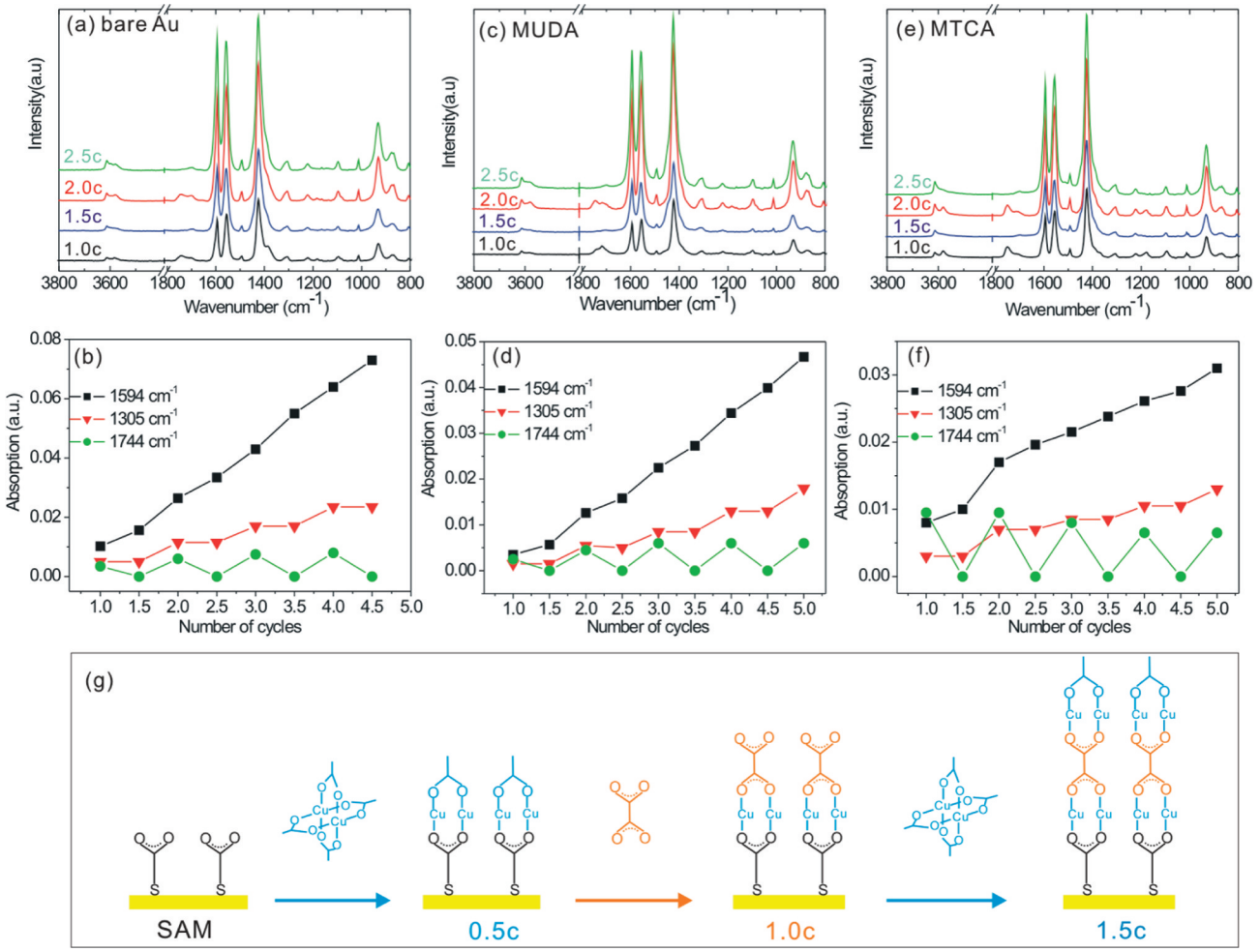

Figure 4. FT-IR spectra of Cu-ADA grown on (a) bare Au, (c) MUDA, and (e) MTCA surfaces at different cycles. "1c" means cycle 1, after which the sample has been immersed once in $Cu_2(OAc)_4$ solution and once in ADA solution, also encoded as 1 $Cu_2(OAc)_4$+ 1 ADA. "1.5c" then designates an additional immersion in $Cu_2(OAc)_4$ solution after cycle 1, describable as 2 $Cu_2(OAc)_4$+ 1 ADA. In analogy 2c and 2.5c refer to 2 $Cu_2(OAc)_4$+ 2 ADA and 3 $Cu_2(OAc)_4$+ 2 ADA, respectively. (b), (d), (f) show the correlation of the intensity of three characteristic peaks in the spectra: 1744 cm^{-1} (−COOH vibration, circles), 1594 cm^{-1} (asymmetric $-COO^-$ vibration, squares), and 1305 cm^{-1} (ADA backbone vibration, triangles) with the number of cycles. To show all the graphs in one plot, the intensities of signals at 1305 cm^{-1} and 1744 cm^{-1} have been multiplied by a factor of 5. (g) The schematic diagram of layer-by-layer growth of Cu-ADA on SAM modified surface.

Obviously at least some of the nanoflakes start to sinter at 523 K, resulting in a lowered accessible surface.

With this morphological information in mind, we tried to figure out the structure of this new material. The energy dispersive X-ray (EDX) spectrum analysis reveals the elemental composition of both nanobrick and nanoflake microspheres to be Cu, O, and C (Supporting Information, Figure S3), as already suggested by the elemental analysis. The powder FT-IR spectra of both kinds of Cu-ADA microspheres are very similar (Supporting Information, Figure S4). The peaks at 1591 cm^{-1} and 1408 cm^{-1} are characteristic absorptions for the asymmetric and symmetric vibrations of the $-COO^-$ group of the ADA ligaznd. The absence of C═O vibrations of −COOH groups (1700−1680 cm^{-1}) reveals that the H_2ADA has been deprotonated completely. The weak, sharp peak(s) at 3613 cm^{-1} (and 3574 cm^{-1} for nanoflake Cu-ADA) are typical for nonassociated −OH groups. These hydroxyl groups might be located at the copper ions and have been described before.[60] In this reference, the formation of OH-bridged Cu−Cu centers has been blamed for the breaking of lateral symmetry, thus hampering the formation of larger crystals, as observed in our case. Joining all the above information together, a very cautious suggestion on the crystal structure of the material may be made: The small cell basically accommodates one ADA^{2-} ligand in its extended (trans) form, with each carboxylate group bridging about two Cu^{2+} ions. These ions may form a chain held together by OH^- ions and H_2O (see Supporting Information, Figure S8). The structure contains many defects, with only 92.5% (bricks) and 96.5% (flakes) Cu^{2+} ions in place, and even less H_2O molecules per unit cell (only about 0.5 to 0.6). This might be the result of steric constraints, which become worse the more Cu^{2+} ions are in the assumed place, distorting the lattice so much that in the case of more than 1.85 Cu^{2+} ions (and their respective OH^- ions) per unit cell, only highly bent thin flakes can be formed.

Since the stepwise layer-by-layer deposition method was developed for growing MOFs thin film, also known as SURMOFs,[29,30] many established MOFs, such as HKUST-1 or MOF-508, have been grown in the form of SURMOFs. Here, we show that the stepwise layer-by-layer deposition method could also be used for growing SURMOFs of the rather new Cu-ADA framework. Figure 4 shows the FT-IR spectra of

dx.doi.org/10.1021/cm2021092 | Chem. Mater. 2011, 23, 5366–5374

Cu-ADA MOF grown either on bare gold surfaces or on SAM surfaces (MUDA and MTCA). At first sight, the growth behavior of those three different surfaces appears to be very similar. All of the pronounced peaks are observed. To study the details of the stepwise growth, we chose three characteristic peaks. Two of them would be expected in the MOF bulk phase, that is, the one at 1594 cm^{-1} (squares in Figure 4 b, d, and f) corresponding to the asymmetric vibration of the $-COO^-$ group and the one at 1305 cm^{-1} (triangles in Figure 4 b, d, and f) being characteristic for the ADA backbone (for comparison, Supporting Information, Figure S9, shows the powder FT-IR spectra of both H_2ADA and ADA^{2-}). It is intuitively clear that the intensity of the latter band shows a staircase-like growth, with an increase only at the completion of the deposition cycles, since only then (at the second immersion step, which is the exposure to the ADA^{2-} solution) the ligand can become deposited at the surfaces. The same can be observed for other signals specific for the ADA ligand, for example, the one at 870 cm^{-1}. In contrast to this, the intensity of the $-COO^-$ vibration (1594 cm^{-1}, squares) shows a linear increase with each of the steps (half-cycles). To understand this, it must be kept in mind that because of the IR selection rules at metallic surfaces,[61] only the vibrations with transition dipole moments perpendicular to the surface become visible. Thus, when the ADA^{2-} ligand is added, only those ligands contribute which stand more or less upright on the surface. By replacing the one acetate ligand at the Cu dimer with this particular orientation by a ADA ligand (carrying two carboxylate groups) the intensity of the signal is increased in proportion of one carboxylate group (see Figure 4 g). The same is true for the attachment of the $Cu_2(OAc)_3$ unit in the first half-cycles: Although effectively three new carboxylate groups become attached per exposed ADA carboxylate group, only the one oriented parallel to the surface normal contributes to the signal (Figure 4 g). Thus a very constant growth of the signal intensity can be observed for the $-COO^-$ vibration at 1594 cm^{-1} (with the exception for the first step on the MTCA surface). Another interesting observation is the alternating appearance/disappearance of a −COOH signal at 1744 cm^{-1}. This signal can only explained by the formation of protonated −COOH groups at the surface of the MOFs, where the general rules for surface chemistries apply. One of the rules describes the increase of the pK_a values of surface-bound acids because of the electrostatic interactions between the respective anions (in this case carboxylates).[62,63] This increase in the pK_a values permits the partial protonation of the carboxylate groups even by pure ethanol, as it was used in the washing steps, thus yielding the weak, but discernible signals at 1744 cm^{-1}. As can be expected, the attachment of the Cu units completely consumes the −COOH groups, making the signal disappear after every half-cycle.

Additionally, the growth was observed by ellipsometric measurements, as presented in Figure 5a. Again, a linear increase of the thickness with each cycle for bare Au, MUDA, and MTCA surfaces could be observed. Nevertheless, the slope of the growth curve varied for each surface (slope I in Table 1). The respective data are presented in Table 1, together with the slopes obtained from the IR measurements mentioned above. All the data reveal that the growth rate of Cu-ADA film descends from bare Au to MUDA to MTCA. This is surprising because −COOH functionalized surfaces usually prefer the deposition of SURMOFs based on di- and tricarboxylate ligands.[20,42] Considering that the length of a Cu-ADA-Cu unit is about 1.7 nm,[53] the Cu-ADA films should only grow by this

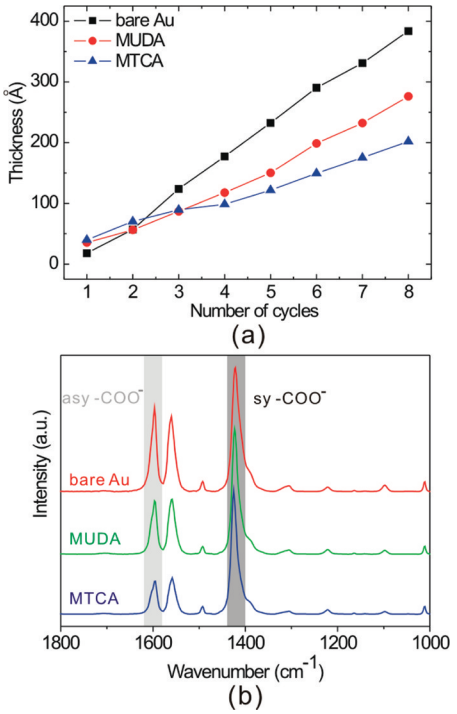

Figure 5. (a) Effective thickness of the Cu-ADA films (determined by ellipsometry) versus number of growth cycles. (b) FT-IR spectra of Cu-ADA film grown on bare Au, MUDA, and MTCA surfaces after 35 cycles. The spectra are normalized to the signal of the symmetric COO^- vibration.

Table 1. Characteristic Growth Parameters for the ADA-Cu MOF on Different Surfaces[a]

surface	slope I (nm/cycle)	slope II (a.u./cycle)	sy/as of COO^-
bare gold	4.7	160	1.3
MUDA	3.3	110	2.2
MTCA	2.5	42	3.8

[a]Slope I is obtained from ellipsometric measurements and slope II is obtained from the peak at 1594 cm^{-1} (asymmetric $-COO^-$ vibration) in FT-IR measurements. The intensity ratios of the signals of the symmetric (1408 cm^{-1}) and asymmetric $-COO^-$ vibration were calculated from the IR spectra after 35 cycles.

value per cycle upon layer-by-layer deposition. This value is only approximately met by the crystals growing on MTCA, but is exceeded by a factor of 2 on MUDA and even a factor of almost three on gold, hinting on multilayer growth. The factors are even larger when the increases of peak intensities for the asymmetric $-COO^-$ vibration (1594 cm^{-1}, slope II in Table 1) are compared on the different surfaces. Here the factor for MUDA is 2.6 and for the bare gold surface almost 4, compared to the increase found on MTCA surface. It has to be kept in mind anyway that the intensity of a surface-IR signal depends not only on the number of the respective groups but also on their orientation, as stated before. Comparison of the intensity of the signal of the asymmetric vibration with the one of the symmetric vibration (the transition dipole moment of which is perpendicular to the one of the former vibration) shows that the asymmetric $-COO^-$ peak (normalized to the signal at 1408 cm^{-1}) is much stronger on bare Au than on MTCA. The FT-IR spectra of Cu-ADA grown on bare Au, MUDA, and MTCA surfaces after 35 cycles are shown in Figure 5b and the respective ratios are presented in Table 1. When compared to

dx.doi.org/10.1021/cm2021092 | Chem. Mater. 2011, 23, 5366–5374

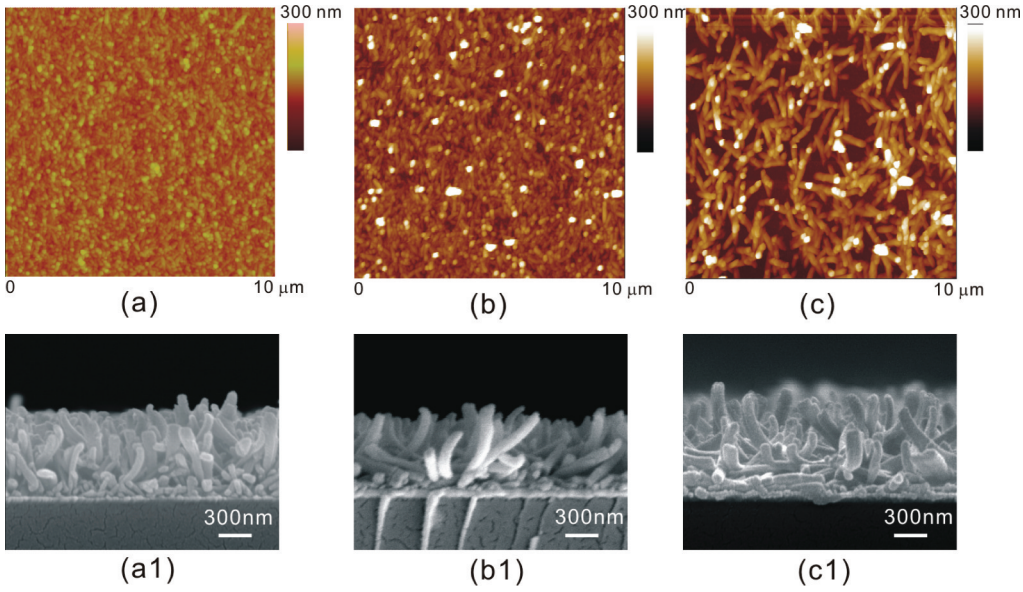

Figure 6. AFM images of Cu-ADA grown on (a) bare Au, (b) MUDA, and (c) MTCA surfaces after 20 cycles. Cross section SEM images of Cu-ADA grown on (a1) bare Au, (b1) MUDA, and (c1) MTCA surfaces after 35 cycles.

the ratio in the nonoriented bulk (1.9 for the nanobrick microspheres), the ratios for the surface films suggest a significant tilt of the ADA units on bare gold, a small preference for the upright orientation on the MUDA-SAMs, and a significant upright orientation of this unit on the MTCA modified surfaces.

To relate this orientational information with the morphology of Cu-ADA deposits, AFM and SEM measurements were performed, as shown in Figure 6a–c. Grains with a size of about 150 nm fully cover the bare Au surface (Figure 6a), resulting in a roughness (rms) of about 15 nm. Interestingly, the morphologies on MUDA and MTCA are remarkably different although both surfaces are terminated with −COOH groups. The Cu-ADA prefers growing as nanorods with a diameter of 200 nm and a length of 1 μm on the MTCA surface (Figure 6c), but with a low density. However, the Cu-ADA on MUDA seems to be a mixture of grains and smaller rods. Our previous study[52] indicated that the COOH-terminated terphenylthiol SAMs are much more ordered than COOH-terminated alkanethiols SAMs because of the rigid backbone. The disordered MUDA surface presumably provides more nucleation sites, causing a higher density of Cu-ADA particles. The lowest density of Cu-ADA nanorods on the MTCA surface also explains the observed slowest growth rate since the thickness measured by ellipsometry is an average thickness. Surprisingly, although AFM suggests that the surface morphologies of Cu-ADA on bare Au, MUDA and MTCA surfaces are different, the cross section SEM images indicate that all the three Cu-ADA thin films consist of nanorods. On the bare Au surface, the nanorods are almost perpendicular to the surface. The grainy surface observed in the respective AFM image is a result of the high density of vertically aligned nanorods. In contrast, the nanorods on the MTCA surface prefer a more tilted orientation on the surface, some of them literally lying down. The white spots in the corresponding AFM image (Figure 6c) represent the few rather upright nanorods.

Importantly, the surface deposited material is in fact identical with the Cu-ADA of the microspheres, as could be demonstrated by the surface XRD patterns. The strong diffraction peak at 2θ = 5.62° from the XRD pattern (Supporting Information, Figure S10) reveals those Cu-ADA thin films are more related to the nanobrick Cu-ADA microspheres (showing the dominant diffraction peak at 2θ = 5.66°) than to the nanoflake ones (with the dominant diffraction peak at 5.37°, see Supporting Information, Figure S1), which might be related to the order forced by the smooth substrate surface, preventing the curving/bending of the crystals typical for the nanoflakes and limiting the copper content to values typical for the nanobricks. Unfortunately, the different orientation of the Cu-ADA crystallites could not be confirmed from the XRD pattern because of the very weak intensity of the diffraction peaks in the range from 12 to 20°.

For the potential application of SURMOFs for smart membranes, sensors, and microelectronic devices, it is critical to control the MOF growth in patterns. SAMs in combination with microcontact printing (μCP) provide a low cost and convenient approach for the patterning of surfaces with various functionalities. When a HDT SAM was deposited as an array of 3 × 3 μm^2 squares, the growth of Cu-ADA was well restricted to the SAM (Figure 7). EDX spectra (Supporting Information, Figure S13) recorded from the square areas verified that the deposit was composed of C, O, and Cu. The preferential

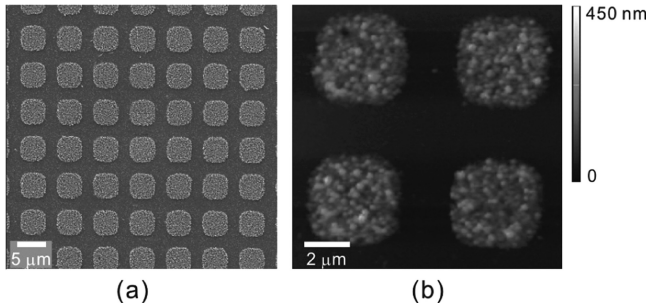

Figure 7. (a) SEM and (b) AFM images of patterned Cu-ADA thin films after 16 cycles deposited on a surface previously patterned by μCP using HDT (squares). No growth was observed on the bare gold surfaces in between.

dx.doi.org/10.1021/cm2021092 | Chem. Mater. 2011, 23, 5366–5374

growth of the MOF at the HDT patches is quite puzzling because these SAMs are usually recognized as chemically inert. It was nevertheless reported before that HKUST-1 shows a faster growth on $-CH_3$ terminated surfaces than on $-COOH$ and $-OH$ terminated surfaces.[35] It has also been reported that crystal nucleation occurs on disordered SAMs much faster than on ordered SAMs.[64] Thus, the disorder in the HDT SAM formed by the μCP procedure might be the reason for the observed Cu-ADA growth. Indeed, when a gold substrate fully covered by HDT (prepared by immersion of the gold substrate in 5 mM HDT solution for 1 h) was used for the stepwise deposition, no Cu-ADA growth was observed. The difference in the order was confirmed by surface IR spectroscopy (Supporting Information, Figure S12): While the fully covered HDT surface shows four sharp peaks stemming from $-CH_3$ (2964 cm^{-1} and 2877 cm^{-1}) and $-CH_2-$ (2929 cm^{-1} and 2850 cm^{-1}) vibrations, the spectra of the patterned HDT surface, in contrast, showed only broad peaks with the one at 2877 cm^{-1} completely missing. Thus, we believe that the disordered HDT surface of the pattern provides more efficient nucleation sites than the bare Au film. The growth on these films is even faster than the one on the bare gold surface. After 16 cycles, the Cu-ADA film had a thickness of about 116 nm, as determined by AFM (Supporting Information, Figure S11), corresponding to a growth rate of 7.2 nm/cycle (bare Au: 4.7 nm/cycle, see Table 1). Apparently, the selectivity of nucleation on patterned surface is a competitive process between different surfaces.

To test this hypothesis, we created a MUDA patterned Au surface. From the data presented in Table 1, we expected that Cu-ADA has higher affinity for the bare gold surface than for the MUDA surface. Indeed, Cu-ADA particles preferentially grew on the bare gold surface (areas between the squares in Supporting Information, Figure S14) and show a high density. Nevertheless, the close-up AFM images show that some Cu-ADA crystals also grew on the $-COOH$-terminated surface (square areas), indicating that the growth competition in fact is there, but is not as pronounced as in the previous case.

CONCLUSIONS

In summary, the MOF formed from copper(II) acetate and azobenzenedicarboxylic acid (H_2ADA) behaved quite unexpectedly in several respects. Instead of substitution of all four of the acetate groups by ADA residues, the elemental composition rather reveals a ratio of Cu(II)/ADA of 2:1. For charge neutrality, the network presumably also contains O^{2-} and OH^- ligands, with the presence of the latter supported by IR spectroscopy. The analysis of the material is facilitated by its nonporous nature, excluding the presence of interfering guest molecules. On the other hand, the material can be tuned regarding its outer surface by adjusting its morphology: Going from nanobrick microspheres to nanoflake microspheres increases its outer surface by almost a factor of 5, as shown by nitrogen sorption experiments and visualized by the adsorption of labeled proteins. This dominance of surface in the nanoflake system becomes also visible in the PXRD, where a signal corresponding to a *d*-spacing characteristic for a relaxed system appears, and in the IR spectra, showing a second set of OH-vibrations.

This material can also be deposited on different surfaces using a stepwise layer-by-layer approach. The surface chemistry primarily influences the orientation of the SURMOF, but also its growth rate. On carboxylic-acid terminated SAMs, the ADA unit stands more upright, as determined by surface IR measurements, while the ADA unit is almost parallel to the surface when grown on bare gold. On the former surface, the crystals preferably are lying down, while on bare gold they are standing basically upright, suggesting a relationship between the orientation of the ADA unit and the one of the crystals. In accordance with this, the order within the carboxyl-terminated SAMs also becomes a corresponding one in the SURMOF, since the orientation becomes more pronounced on the highly ordered MTCA SAM than on the notoriously disordered MUDA SAM.[52] The order in the SAM also influences the nucleation rate and even the growth rate on the surfaces. Thus, an alkanethiol SAM (HDT) deposited by μCP, for which the disorder was demonstrated by IR, permitted the preferential growth in comparison to the neighboring gold surface, while on a highly ordered HDT SAM no growth at all could be induced. These observations open the door for a very directed manipulation of the growth location and orientation of Cu-ADA and presumably other kinds of SURMOFs.

ASSOCIATED CONTENT

Supporting Information

Additional spectroscopic data, microscopic data, PXRD, and TGA (PDF). This material is available free of charge via the Internet at http://pubs.acs.org.

AUTHOR INFORMATION

Corresponding Author

*E-mail: aterfort@chemie.uni-frankfurt.de.

ACKNOWLEDGMENTS

This project was supported in its initial phase by the EU through the FP6 STREP initiative "SURMOF". J.L.Z. and A.T. gratefully acknowledge financial support by the Beilstein-Institut, Frankfurt/Main, Germany, within the research collaboration NanoBiC. U.K. and I.A. gratefully acknowledge financial support by the DFG, SPP1415. We thank Dr. L. Fink, Frankfurt, for the help with the acquisition of the PXRD data and Dr. T. Henning (Mikro-/Nanolabor, Gießen) for assisting with the SE microscopy. The generous gift of gold granules by Aurubis is thankfully acknowledged.

REFERENCES

(1) Murray, L. J.; Dinca, M.; Long, J. R. *Chem. Soc. Rev.* **2009**, *38*, 1294−1314.
(2) Lee, J.; Farha, O. K.; Roberts, J.; Scheidt, K. A.; Nguyen, S. T.; Hupp, J. T. *Chem. Soc. Rev.* **2009**, *38*, 1450−1459.
(3) Chen, X. D.; Wan, C. Q.; Sung, H. H. Y.; Williams, I. D.; Mak, T. C. W. *Chem.—Eur. J.* **2009**, *15*, 6518−6528.
(4) Kitagawa, S.; Kitaura, R.; Noro, S. *Angew. Chem., Int. Ed.* **2004**, *43*, 2334−2375.
(5) Tranchemontagne, D. J.; Mendoza-Cortes, J. L.; O'Keeffe, M.; Yaghi, O. M. *Chem. Soc. Rev.* **2009**, *38*, 1257−1283.
(6) Farha, O. K.; Hupp, J. T. *Acc. Chem. Res.* **2010**, *43*, 1166−1175.
(7) Kitagawa, S.; Matsuda, R. *Coord. Chem. Rev.* **2007**, *251*, 2490−2509.
(8) Li, H.; Eddaoudi, M.; O'Keeffe, M.; Yaghi, O. M. *Nature* **1999**, *402*, 276−279.
(9) Livage, C.; Egger, C.; Ferey, G. *Chem. Mater.* **1999**, *11*, 1546−1550.
(10) Maspoch, D.; Ruiz-Molina, D.; Wurst, K.; Domingo, N.; Cavallini, M.; Biscarini, F.; Tejada, J.; Rovira, C.; Veciana, J. *Nat. Mater.* **2003**, *2*, 190−195.
(11) Rosseinsky, M. J. *Microporous Mesoporous Mater.* **2004**, *73*, 15−30.

(12) Keskin, S.; Kizilel, S. *Ind. Eng. Chem. Res.* **2011**, *50*, 1799−1812.
(13) Ni, Z.; Masel, R. I. *J. Am. Chem. Soc.* **2006**, *128*, 12394−12395.
(14) Jhung, S. H.; Lee, J. H.; Yoon, J. W.; Serre, C.; Ferey, G.; Chang, J. S. *Adv. Mater.* **2007**, *19*, 121−124.
(15) Qiu, L. G.; Li, Z. Q.; Wu, Y.; Wang, W.; Xu, T.; Jiang, X. *Chem. Commun.* **2008**, 3642−3644.
(16) Li, Z. Q.; Qiu, L. G.; Xu, T.; Wu, Y.; Wang, W.; Wu, Z. Y.; Jiang, X. *Mater. Lett.* **2009**, *63*, 78−80.
(17) Taylor, K. M. L.; Jin, A.; Lin, W. B. *Angew. Chem., Int. Ed.* **2008**, *47*, 7722−7725.
(18) Rieter, W. J.; Taylor, K. M. L.; An, H. Y.; Lin, W. L.; Lin, W. B. *J. Am. Chem. Soc.* **2006**, *128*, 9024−9025.
(19) Spokoyny, A. M.; Kim, D.; Sumrein, A.; Mirkin, C. A. *Chem. Soc. Rev.* **2009**, *38*, 1218−1227.
(20) Zhuang, J. L.; Ceglarek, D.; Pethuraj, S.; Terfort, A. *Adv. Funct. Mater.* **2011**, *21*, 1442−1447.
(21) Sun, X. P.; Dong, S. J.; Wang, E. K. *J. Am. Chem. Soc.* **2005**, *127*, 13102−13103.
(22) Imaz, I.; Hernando, J.; Ruiz-Molina, D.; Maspoch, D. *Angew. Chem., Int. Ed.* **2009**, *48*, 2325−2329.
(23) Imaz, I.; Maspoch, D.; Rodriguez-Blanco, C.; Perez-Falcon, J. M.; Campo, J.; Ruiz-Molina, D. *Angew. Chem., Int. Ed.* **2008**, *47*, 1857−1860.
(24) Tsuruoka, T.; Furukawa, S.; Takashima, Y.; Yoshida, K.; Isoda, S.; Kitagawa, S. *Angew. Chem., Int. Ed.* **2009**, *48*, 4739−4743.
(25) Lu, W.; Chui, S. S. Y.; Ng, K. M.; Che, C. M. *Angew. Chem., Int. Ed.* **2008**, *47*, 4568−4572.
(26) Carne, A.; Carbonell, C.; Imaz, I.; Maspoch, D. *Chem. Soc. Rev.* **2011**, *40*, 291−305.
(27) Dekrafft, K. E.; Xie, Z. G.; Cao, G. H.; Tran, S.; Ma, L. Q.; Zhou, O. Z.; Lin, W. B. *Angew. Chem., Int. Ed.* **2009**, *48*, 9901−9904.
(28) Zacher, D.; Shekhah, O.; Wöll, C.; Fischer, R. A. *Chem. Soc. Rev.* **2009**, *38*, 1418−1429.
(29) Zacher, D.; Schmid, R.; Wöll, C.; Fischer, R. A. *Angew. Chem., Int. Ed.* **2011**, *50*, 176−199.
(30) Shekhah, O.; Liu, J.; Fischer, R. A.; Wöll, C. *Chem. Soc. Rev.* **2011**, *40*, 1081−1106.
(31) Li, Y. S.; Liang, F. Y.; Bux, H.; Feldhoff, A.; Yang, W. S.; Caro, J. *Angew. Chem., Int. Ed.* **2010**, *49*, 548−551.
(32) Li, Y. S.; Bux, H.; Feldhoff, A.; Li, G. L.; Yang, W. S.; Caro, J. *Adv. Mater.* **2010**, *22*, 3322−3326.
(33) Lu, G.; Hupp, J. T. *J. Am. Chem. Soc.* **2010**, *132*, 7832−7833.
(34) Hermes, S.; Schröder, F.; Chelmowski, R.; Wöll, C.; Fischer, R. A. *J. Am. Chem. Soc.* **2005**, *127*, 13744−13745.
(35) Biemmi, E.; Scherb, C.; Bein, T. *J. Am. Chem. Soc.* **2007**, *129*, 8054−8055.
(36) Ranjan, R.; Tsapatsis, M. *Chem. Mater.* **2009**, *21*, 4920−4924.
(37) Demessence, A.; Horcajada, P.; Serre, C.; Boissiere, C.; Grosso, D.; Sanchez, C.; Ferey, G. *Chem. Commun.* **2009**, 7149−7151.
(38) Horcajada, P.; Serre, C.; Grosso, D.; Boissiere, C.; Perruchas, S.; Sanchez, C.; Ferey, G. *Adv. Mater.* **2009**, *21*, 1931−1935.
(39) Shekhah, O.; Wang, H.; Paradinas, M.; Ocal, C.; Schüpbach, B.; Terfort, A.; Zacher, D.; Fischer, R. A.; Wöll, C. *Nat. Mater.* **2009**, *8*, 481−484.
(40) Shekhah, O.; Wang, H.; Zacher, D.; Fischer, R. A.; Wöll, C. *Angew. Chem., Int. Ed.* **2009**, *48*, 5038−5041.
(41) Zacher, D.; Yusenko, K.; Betard, A.; Henke, S.; Molon, M.; Ladnorg, T.; Shekhah, O.; Schüpbach, B.; de los Arcos, T.; Krasnopolski, M.; Meilikhov, M.; Winter, J.; Terfort, A.; Wöll, C.; Fischer, R. A. *Chem.—Eur. J.* **2011**, *17*, 1448−1455.
(42) Shekhah, C.; Wang, H.; Kowarik, S.; Schreiber, F.; Paulus, M.; Tolan, M.; Sternemann, C.; Evers, F.; Zacher, D.; Fischer, R. A.; Wöll, C. *J. Am. Chem. Soc.* **2007**, *129*, 15118−15119.
(43) Ameloot, R.; Stappers, L.; Fransaer, J.; Alaerts, L.; Sels, B. F.; De Vos, D. E. *Chem. Mater.* **2009**, *21*, 2580−2582.
(44) Schoedel, A.; Scherb, C.; Bein, T. *Angew. Chem., Int. Ed.* **2010**, *49*, 7225−7228.
(45) Makiura, R.; Motoyama, S.; Umemura, Y.; Yamanaka, H.; Sakata, O.; Kitagawa, H. *Nat. Mater.* **2010**, *9*, 565−571.
(46) Motoyama, S.; Makiura, R.; Sakata, O.; Kitagawa, H. *J. Am. Chem. Soc.* **2011**, *133*, 5640−5643.
(47) Makiura, R.; Kitagawa, H. *Eur. J. Inorg. Chem.* **2010**, *24*, 3715−3724.
(48) Ameloot, R.; Gobechiya, E.; Uji-i, H.; Martens, J. A.; Hofkens, J.; Alaerts, L.; Sels, B. F.; De Vos, D. E. *Adv. Mater.* **2010**, *22*, 2685−2688.
(49) Chisholm, M. H.; D'Acchioli, J. S.; Hadad, C. M.; Patmore, N. J. *Inorg. Chem.* **2006**, *45*, 11035−11042.
(50) Ballav, N.; Thomas, H.; Winkler, T.; Terfort, A.; Zharnikov, M. *Angew. Chem., Int. Ed.* **2009**, *48*, 5833−5836.
(51) Raiber, K.; Terfort, A.; Benndorf, C.; Krings, N.; Strehblow, H. H. *Surf. Sci.* **2005**, *595*, 56−63.
(52) Himmel, H. J.; Terfort, A.; Wöll, C. *J. Am. Chem. Soc.* **1998**, *120*, 12069−12074.
(53) Reineke, T. M.; Eddaoudi, M.; Moler, D.; O'Keeffe, M.; Yaghi, O. M. *J. Am. Chem. Soc.* **2000**, *122*, 4843−4844.
(54) Chen, B. L.; Ma, S. Q.; Hurtado, E. J.; Lobkovsky, E. B.; Zhou, H. C. *Inorg. Chem.* **2007**, *46*, 8490−8492.
(55) Furukawa, H.; Kim, J.; Ockwig, N. W.; O'Keeffe, M.; Yaghi, O. M. *J. Am. Chem. Soc.* **2008**, *130*, 11650−11661.
(56) Bhattacharya, S.; Sanyal, U.; Natarajan, S. *Cryst. Growth Des.* **2011**, *11*, 735−747.
(57) Kolb, U.; Gorelik, T.; Kübel, C.; Otten, M. T.; Hubert, D. *Ultramicroscopy* **2007**, *107*, 507−513.
(58) Kolb, U.; Gorelik, T.; Otten, M. T. *Ultramicroscopy* **2008**, *108*, 763−772.
(59) Kolb, U.; Mugnaioli, E.; Gorelik, T.; Stewart, A. *Polym. Rev.* **2010**, *50*, 385−409.
(60) Kanoo, P.; Gurunatha, K. L.; Maji, T. K. *J. Mater. Chem.* **2010**, *20*, 1322−1331.
(61) Born, M.; Wolf, E. *Principles of Optics*, 2nd ed.; Cambridge University Press: Cambridge, U.K., 1999.
(62) Hu, K.; Bard, A. J. *Langmuir* **1997**, *13*, 5114−5119.
(63) Bain, C. D.; Whitesides, G. M. *Langmuir* **1989**, *5*, 1370−1378.
(64) Aizenberg, J. *J. Chem. Soc., Dalton Trans.* **2000**, 3963−3968.